RSC Advances

ROYAL SOCIETY OF CHEMISTRY

www.rsc.org/advances

RSC Advances

RSC**Publishing**

COMMUNICATION

Enhanced Field Emission Properties Based on In-In$_2$O$_3$ Composite Nanopagodas

Sin-Hui Wang[a], Shin Liu[a], Shoou-Jinn Chang*[a], Tsung-Ying Tsai[a], Cheng-Liang Hsu*[b]

The In-In$_2$O$_3$ composite nanopagodas preform excellent field emission properties with enhanced kinetics factor (saturation ratio). The turn-on fields and β of In-In$_2$O$_3$ nanopagodas were 2.0V/µm and 3590. The indium of In-In$_2$O$_3$ nanopagodas was accumulates electrons point and form electrons tunnelled, which enhanced the performance of field emission properties.

Introduction

Recently, In$_2$O$_3$ has been attracted much attention on the wide direct bandgap energy of 3.4-3.8 eV,[1,2] and now widely used in field-emission, gas sensors and solar cells.[3-5] It is well known that the optical and electronic properties of metal oxide semiconductor can be modulated by various morphology or doped variety element. For the morphology of In$_2$O$_3$, there are various appearances of one-dimensional (1D) In$_2$O$_3$ nanostructures have been made, including nanotubes, nanowires (NWs), nanobelts, nanorods, etc.[6-8]

The 1D nanostructures (NSs) have attracted considerable interest for their potential applications in field emission (FE) because of their sharp tips and high aspect ratio, which cause their high field enhancement factor (β).[9] Li *et al.* reported the electric-filed-aligned vertical and randomly growth of In$_2$O$_3$ NWs.[10] Kar *et al.* reported that nanopyramids, nanocolumns and NWs of In$_2$O$_3$.[11] Thus, investigated of the FE properties of the In$_2$O$_3$ 1D nanoforms were the key factors.

According to Huang *et al.* reported four kinds of novel layered In$_2$O$_3$ NSs were synthesized by controlling the kinetics factor (saturation ratio).[12] In this paper, two kinds of In$_2$O$_3$ NSs were synthesized by changing the directions of the substrate. In addition to decrease the distance between the metal source and substrate, we demonstrate the first successful fabrication of In-In$_2$O$_3$ conformable nanopagodas (NPs). The FE properties of In-In$_2$O$_3$ NPs was better than In$_2$O$_3$ NWs.

Experimental

A 500-nm-thick silicon dioxide (SiO$_2$) insulating layer was deposited onto a Si (111) substrate by wet oxidation. A 3-nm-thick Au film as the catalyst layer was deposited onto the SiO$_2$/Si substrate by electron-beam evaporator. Thermal vapor deposition was performed for the vapor-liquid-solid (VLS) method growth of In$_2$O$_3$ NSs. About 0.3 g In powder (99.993%) was poured into an alumina bowl. The bowl, filled with powder, was placed in the center of an alumina boat. Placed the Au/SiO$_2$/Si substrate next to the alumina bowl, and reversed the substrate which was covered upon the alumina boat. The argon flow rate was maintained at 54.4 sccm and the oxygen was with a flow rate of 0.3 sccm. During the growth of In$_2$O$_3$, the quartz tube pressure, growth temperature, and growth time were maintained at 8 torr, 1000 ˚C, and 30 min, respectively. For enhanced the saturation ratio, we changed the placement of the substrate beside and upon the indium metal source bowl in the horizontal quartz furnace.

The morphologies and size distribution of the as-grown In$_2$O$_3$ NSs were characterized using a field-emission scanning electron microscope (FESEM) (JSM-7000F), which was operated at 10 keV. The crystallographic and structural properties of the as-grown In$_2$O$_3$ NSs were then determined using a MACMXP18 X-ray diffractometer. The field emission (FE) properties of these In$_2$O$_3$ NSs at room temperature in a vacuum chamber at a pressure of 4×10^{-6} Torr. During FE measurements, the anode was a tungsten probe with a diameter of 1.8 mm, while the inter electrode distance d between the anode and the In$_2$O$_3$ NSs was precisely maintained at 150 µm. The lamp was placed above the Si substrate as an excitation source for the In$_2$O$_3$ NSs. The current–voltage ($I-V$) characteristics were determined using a Keithley 237 high-voltage source and measuring unit, which measured in femtometers and provided a maximum voltage of 1000V. The FE properties were extracted from the obtained $I-V$ curves using the Fowler–Nordheim ($F-N$) model.

Results and Discussion

Figure 1(a) shows the cross-sectional FESEM image by fronted the Au/SiO$_2$/Si substrate with the morphology of In$_2$O$_3$ NWs. The diameter and length of the In$_2$O$_3$ NWs were 100 nm and 12~18 µm. For enhanced the vapor pressure of metal, we reversed the location of substrates above the Indium powers, and got the In-In$_2$O$_3$ NPs, as shown in **Figure 1(b)**. The diameter and length of the In-In$_2$O$_3$ NPs were 0.1~1 µm and 3~6 µm. According to the energy-dispersive X-ray (EDX) spectrum of the In$_2$O$_3$ NWs and In-In$_2$O$_3$ NPs, the In : O were 1.8 : 3 and 2.3 : 3, as shown in **Figure 1(c)** and **(d)**. We could

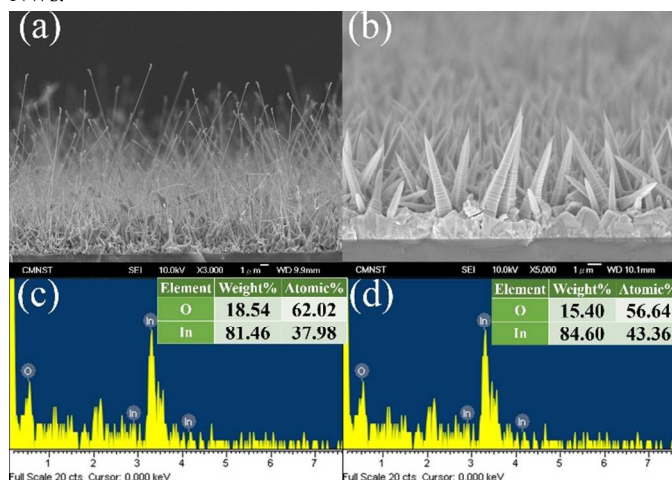find out the content of In in In-In$_2$O$_3$ NPs was higher than in In$_2$O$_3$ NWs.

Figure 1 FESEM images and EDS of In$_2$O$_3$ NSs synthesized at 1000 °C with the position of substrate **(a)**, **(c)** beside and **(b)**, **(d)** upon the precursor.
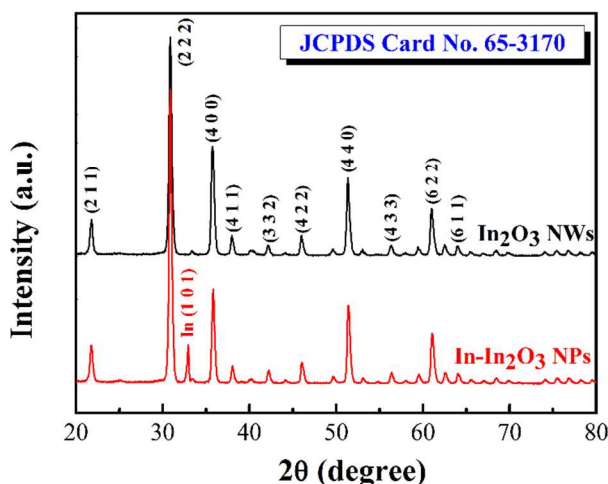

Figure 2 X-ray diffraction indexed, revealing the In$_2$O$_3$ NWs and In-In$_2$O$_3$ NPs.

The lattice structure analysis was performed by the XRD measurement in this section. **Figure 2** shows the XRD 2θ-scan spectrum. The black line represents the XRD result of the In$_2$O$_3$ NWs we synthesized before and reveals a body-centred cubic (bcc) structure with a lattice constant of a = 10.09 Å was characterized by JCPDS card no. 65-3170. Other peaks are also represented to In$_2$O$_3$ structure by JCPDS database and indicated in the spectrum. These weaker peaks were thought to be the resultant causing by the thin layer or particles depositing on the surface at the initial growth process. The red line represents the XRD result of the In-In$_2$O$_3$ NPs. The peak (222) is strengthened in In-In$_2$O$_3$ NPs. The quite strengthened peak of (222) is ascribed to lateral 0-D growth of the In-In$_2$O$_3$ NPs as describing in the previous growth process. As shown in spectrum, the other difference is that there is a peak represented to pure indium by JCPDS card no. 85-1409. The metal of indium was really existed in the In-In$_2$O$_3$ NPs, and it is worth pointing out that the other peaks represented to In-In$_2$O$_3$ NPs structure have no shift as comparing with database and comes to the conclusion that In$_2$O$_3$ NWs fabricated in this study are characteristic of fine crystal structure.

In the production process of In$_2$O$_3$ NWs, the substrate was placed next to the indium power boat, the Au film on SiO$_2$/Si

substrate would form the Au nanoparticles at around 500 °C. The Au nanoparticles acted as the catalysts of VLS growth. Due to larger amount of indium vapors reacting with oxygen, the oxidized indium vapors were with a conspicuous supersaturation ratio. Research had shown that the supersaturation ratio is inversely proportional to the critical core radius.[13] Additionally, the eutectic droplets acted as the absorption sites for oxidized indium vapors and confined these precipitates to one-dimension growth. At higher temperature, indium vapors would be notably generated and abundant reagent species would be adsorbed onto the droplets. It could lead to the rapid precipitating of solid In$_2$O$_3$ NSs and the reaction would take place at the liquid-solid for maintaining the 1D growth.
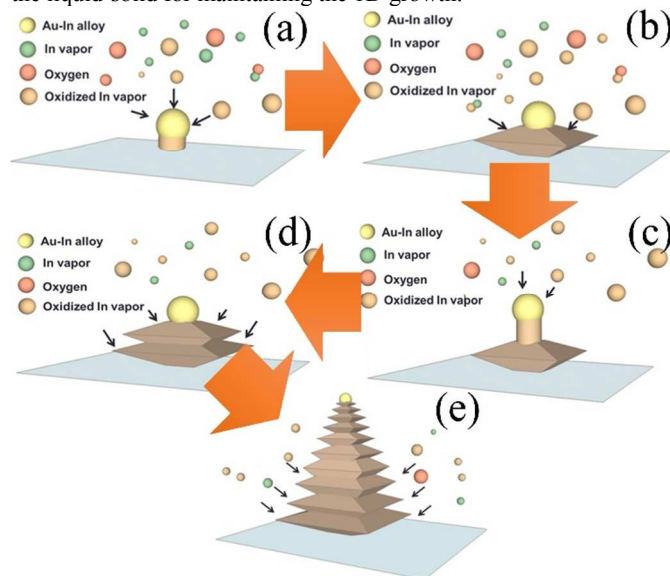

Figure 3 Growth process of In-In$_2$O$_3$ NPs.

The synthesis of the In-In$_2$O$_3$ NPs during the growth process was carried out as the evolution described in **Figure 3** and three different mechanisms were ascribed to the formation of In-In$_2$O$_3$ NPs.

(I) To begin with the evaporation of liquid indium, some indium vapors would directly deposit and alloy with the Au nanoparticles before oxidizing due to the short distance between the substrate and the precursor. So, the composition of the eutectic droplet would mainly be indium, played the catalytic role of the growth mechanism. Abundant In vapors reacted with oxygen as temperature rising and dissolved into the alloy droplet continuously. Once the vapor pressure of these adsorbed species in the droplet reaching supersaturation vapor pressure, the consequent 1-D growth mechanism of solid-state In$_2$O$_3$ would start as shown in **Figure 3(a)**.

(II) As growth time went by, gradual decreasing of the saturation ratio of reagent species would slow down the rate of 1-D growth. It was at this stage the continuous indium vapors evaporated from the precursor would be oxidized and adsorbed onto the surface of 1-D In$_2$O$_3$ NS. Considering the low saturation ratio of adsorbed species in the droplet, it was too less to maintain the mechanism of 1-D growth. As a result, these abundant oxidized indium vapors would prefer to 0-D growth following by vapor-solid (V-S) mechanism.[14] Subsequently, the lateral growth would carry on as shown in **Figure 3(b).**

(III) During the 0-D growth process, there was some oxidized indium vapors dissolved into the catalytic droplet at the top. Moreover, the reagent species adsorbed on the lateral surface might also diffused into the droplet. So, the saturation ratio would rise gradually and reach the supersaturation vapor pressure. The VLS mechanism then dominated the growth process once again. As a

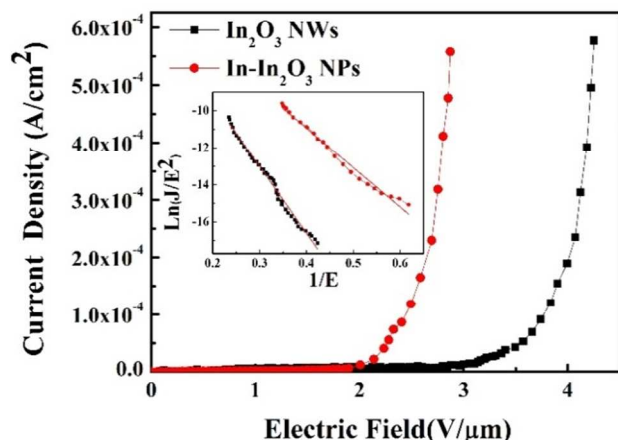result, most of the adsorbed species would transfer to maintain the 1-D growth as **Figure 3(c)** shown.

Figure 4 The J-E field emission plot of the In_2O_3 NWs and In-In_2O_3 NPs. The inset displays the F-N plots of $ln(J/E^2)$ versus $1/E$.

(IV) Again, if the saturation ratio was gradually lowered, it would turn back to the 0-D growth mechanism as described in step II and lateral growth restarted as shown in **Figure 3(d)**. Based on the varied saturation ratio of the droplet, the whole growth process had the competitive phenomenon between longitudinal 1-D growth and the radial 0-D growth as shown in Figure 3(e). Worthy mentioning, even when it was dominated by 1-D growth, there was still some reagent species diffusing to the lateral surface. Consequently, it caused the lateral growth uninterrupted during the whole growth process. So, if the lateral layer of the NPs was closer to the bottom, it was characteristic of the large diameter because of the longer growth time.

Figure 4 plots the FE current density (J) of the In_2O_3 NWs as a function of the applied electric field (E). The turn-on field (E_{to}) is defined as an electric field producing a current density of 10 μA/cm^2. The E_{to} of In_2O_3 NWs and In-In_2O_3 NPs are 2.9 and 2.0 V/μm. The $ln(J/E^2)$ was replotted as a function of $1/E$ in the F-N plot in the inset in Figure 4. The FE property was analyzed by F-N theory to understand the emission characteristics, using the following equation:

$$J = \left(\frac{AE^2\beta^2}{\Phi}\right)exp\left(\frac{-B\Phi^{3/2}}{E\beta}\right)$$

where E was the applied field; V represented the applied voltage; Φ was the work function; β was so-called field enhancement factor which is principally related to the emitter geometry; A and B are constants with the values of 1.56×10^{-6} A eV V^{-2} and 6.83×10^3 eV$^-$ $^{3/2}$V μm^{-1}, respectively.[15-17] The slope of the FN plot was a function of both β and Φ, expressed as:

$$slope = \frac{B\Phi^{\frac{3}{2}}}{\beta}$$

which could be used to calculate the field enhancement factor or the work function. Assuming that the work function is 5.0 eV for In_2O_3, the field enhancement factors of In_2O_3 NWs were estimated to be about 2123, respectively. When the saturation ratio increased, the In_2O_3 NS transformed into In-In_2O_3 NPs and the β was enhanced to 3590.
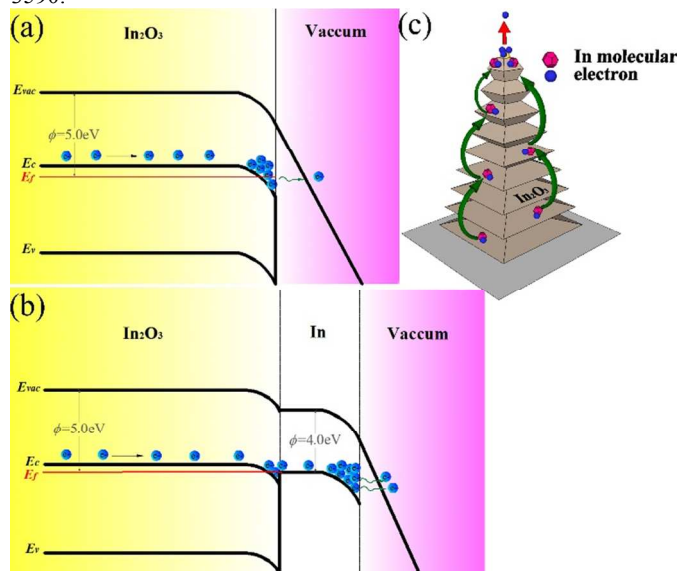

Figure 5 Band diagrams of **(a)** In_2O_3 NWs and **(b)** In-In_2O_3 NPs. **(c)** The schematic diagram of the electronic transmission channel in In-In_2O_3 NPs.

In **Table 1**, the In_2O_3 nanotowers displayed the highest E_{to} value and was depended on the tip diameter.[18] Lin *et al.* reported β values are related to the emitter geometry, crystal structure, vacuum gaps, and spatial distribution of emitting centers.[21] It shows that β obviously depends on d with a relationship of $1/\beta$ proportional to $1/d$. According to above two viewpoints, in this work, the E_{to} and β values of In_2O_3 NWs and In-In_2O_3 NPs are lower and higher than references in **Table 1**. However, In_2O_3 NWs and In-In_2O_3 NPs in this report have the same tip diameter and d, we attribute to the metal indium in the In-In_2O_3 NPs will enhance the transmission of electrons.

Table 1 Comparative key FE performance parameters of the present In-In_2O_3 NPs and conventional In_2O_3 NSs reported in the literature. (The E_{to} is defined as an electric field producing a current density of 10 μA/cm^2.)

material	length (μm)	tip diameter (nm)	d (μm)	E_{to} (V/μm)	β	Ref.
In-In_2O_3 nanopagodas	3 ~ 6	100	150	2.0	3590	this work
In_2O_3 nanowires	12 ~ 18	100		2.88	2123	
In_2O_3 nanoneedles	2	50		4.9	3695	
nanohooks	several tens	50	300	7.5	1770	16
nanorods	several tens	125		7.7	1374	
nanotowers	several tens	300		9.5	458	
In_2O_3 nanotree	several tens	few micrometers		6.45	1993	
nanopin	> 300	1000	220	4.58	2320	17
nanobrush	> 400	600		3.94	2749	
Sn-In_2O_3 nanowires	5	50	X	6.6	1857	18
In_2O_3 nanowires - Ga_2O_3 nanobelt	60	300	170	4.23	1142	19

Figure 5(a) schematically depicts the band diagrams of the tips of In_2O_3 NWs. In_2O_3 is an n-type material. The Fermi level (E_f) of the depletion region was close to the conduction band E_c. When in high electric field, the conduction band bends to E_f, and the electrons will tunnel to the vacuum level. In accordance with the metal indium enhance FE performance, the band diagrams of In-In_2O_3 NPs show in **Figure 5(b)**. In **Figure 5(c)**, the electrons were come from electrical power and then transport from In_2O_3 NPs to metal In region. The In clusters of In_2O_3 NPs assembled many transfer paths for enhanced conductivity. Ultimately the electrons collected at Au-In alloy nanoparticles (the tips of In-In_2O_3 NPs) by electric field effect. The work function of In_2O_3, Au and In are 5.0 eV, 5.1 eV and 4.0 eV, respectively[22]. The electrons tunnel from In region to vacuum level will be easier than Au and In_2O_3. The enhance performance of In-In_2O_3 NPs FE properties come from In clusters assembled conduction paths and reduced work function Φ. This work reveals the lowest E_{to} and the best FE performance compared with past In_2O_3 nanostructures reports.

Conclusions

The morphology of In_2O_3 NSs was transformed from NWs into NPs with In vapor pressure increased. The In-In_2O_3 conformable NPs were synthesized with ultrahigh concentrations of indium vapor. The turn-on fields of In_2O_3 NWs and In-In_2O_3 NPs were 2.9 and 2.0 V/μm, respectively. In-In_2O_3 NPs increased the β value to 3590, separating the β of novel In_2O_3 NWs was 2123. The In clusters in In-In_2O_3 NPs acts the electrons transmission channels and FE emitter due to its lower work function Φ. The In-In_2O_3 NPs presents the best FE properties of In_2O_3 NSs group reports and it is a suitable candidate for FE sensitive switching elements in nanoelectronic device applications.

Acknowledgments

Notes and references

[a] Institute of Microelectronics & Department of Electrical Engineering Center for Micro/Nano Science and Technology Advanced Optoelectronic Technology Center National Cheng Kung University, Tainan, 701, Taiwan, ROC.; E-mail: changsj@mail.ncku.edu.tw

[b] Department of Electrical Engineering, National University of Tainan, Tainan 700, Taiwan, ROC. Fax: +886-6-2602305; Tel: +886-6-2606123 #7785; E-mail: clhsu@mail.nutn.edu.tw

1 H. A. R. Aliabad, Y. Asadi and I. Ahmad, *Opt. Mater.*, 2012, **34**, 1406.

2 Y. Fan, M. Jin, F. Xianjin and K. Lingyi, *J. Cryst. Growth*, 2008, **310**, 4054.

3 S. Q. Li, Y. X. Liang, and T. H. Wang, *Appl. Phys. Lett.*, 2005, **87**, 143104.

4 P. S. Khiabani, E. Marzbanrad, H. Hassani and B. Raissi, *J. Am. Ceram. Soc.*, 2013, **96**, 2493.

5 D. H. Kim, S. Lee, J. H. Park, J. H. Noh, I. J. Park, W. M. Seong and K. S. Hong, *Sol. Energy Mater. Sol. Cells*, 2012, **96**, 276.

6 L. Xu, B. A. Dong, Y. Wang, X. Bai, Q. Liu and H. W. Song, *Sens. Actuators, B*, 2010, **147**, 531.

7 G. Z. Shen, J. Xu, X. F. Wang, H. T. Huang and D. Chen, *Adv. Mater.*, 2011, **23**, 771.

8 J. Yang, C. K. Lin, Z. L. Wang and J. Lin, *Inorg. Chem.*, 2006, **45**, 8973.

9 K.F. Huo, X. M. Zhang, L. S. Hu, X. Sun1, J. Fu1 and P. K. Chu, *Appl. Phys. Lett.*, 2008, **93**, 013105.

10 S. Q. Li, Y. X. Liang and T. H. Wang, *Appl. Phys. Lett.*, 2005, **87**, 143104.

11 S. Kar, S. Chakrabarti and S. Chaudhuri, *Nanotechnology*, 2006, **17**, 3058.

12 S. Jeong, J. Y. Lee, S. S. Lee, Y. Choi and B. H. Ryu, *J. Phys. Chem. C*, 2011, **115**, 11773.

13 Y. Hao, G. Meng, C. Ye, and L. Zhang, *Cryst. Growth Des.*, 2005, **5**, 617.

14 Y. G. Yan, Y. Zhang, H. B. Zeng, and L. D. Zhang, *Cryst. Growth Des.*, 2007, **7**, 940.

15 R. H. Fowler and L. Nordheim, *Proc. R. Soc. Lond. A*, 1928, **119**, 173.

16 C. J. Edgcombe, *Philosophical Magazine Part B*, 2002, **82**, 1009.

17 V. Filip, D. Nicolaescu, M. Tanemura and F. Okuyama, *Ultramicroscopy*, 2001, **89**, 39.

18 B. Wang, X. Jin, Z. B. Ouyang and P. Xu, *J. Nanopart. Res.*, 2012, **14**, 1008.

19 Y. Wang, Y. Li, K. Yu and Z. Zhu, *J. Phys. D: Appl. Phys.*, 2011, **44**, 105301.

20 W. C. Chang, C. H. Kuo, C. C. Juan, P. J. Lee, Y. L. Chuh and S. J. Lin, *Nanoscale Res. Lett.*, 2012, **7**, 684.

21 J. Lin, Y. Huang, Y. Bando, C. C. Tang, C. Li and D. Golberg, *Acs Nano*, 2010, **4**, 2452.

22 S. Kar, S. Chakrabarti, and S. Chaudhuri, *Nanotechnology*, 2006, **17**, 3058.

RSC Advances Accepted Manuscript